

# LAMA: Stable Dual-Domain Deep Reconstruction For Sparse-View CT

Chi Ding, Qingchao Zhang, Ge Wang, *Fellow, IEEE*, Xiaojing Ye, and Yunmei Chen, *Member, IEEE*

**Abstract**—Inverse problems arise in many applications, especially tomographic imaging. We develop a Learned Alternating Minimization Algorithm (LAMA) to solve such problems via two-block optimization by synergizing data-driven and classical techniques with proven convergence. LAMA is naturally induced by a variational model with learnable regularizers in both data and image domains, parameterized as composite functions of neural networks trained with domain-specific data. We allow these regularizers to be nonconvex and nonsmooth to extract features from data effectively. We minimize the overall objective function using Nesterov’s smoothing technique and residual learning architecture. It is demonstrated that LAMA reduces network complexity, improves memory efficiency, and enhances reconstruction accuracy, stability, and interpretability. Extensive experiments show that LAMA significantly outperforms state-of-the-art methods on popular benchmark datasets for Computed Tomography.

**Index Terms**—inverse problems, alternating minimization, convergence, neural networks, stability, interpretability, computed tomography.

## I. INTRODUCTION

DEEP learning (DL) has transformed various fields, including computer vision and image processing, by efficiently extracting features from input images. Recently, DL techniques for tomographic image reconstruction have attracted significant attention. Sparse-view CT (SVCT), which performs undersampled tomographic scans to minimize radiation exposure while maintaining diagnostic accuracy, has emerged as a solution to address concerns about radiation risks in medical imaging. Following the ALARA principle, SVCT has been a focal point in medical imaging research, albeit introducing noise and artifacts into reconstructed images. To tackle this, noise reduction methods in SVCT are categorized into sinogram filtration, iterative reconstruction, and image post-processing [1], each with its limitations and advantages. While sinogram filtration methods utilize noise characteristics, they often suffer from edge blurring. Iterative techniques optimize objective functions but are time-consuming and require empirical adjustment of hyperparameters. Image post-

processing directly manipulates reconstructed images, offering accessibility but subject to patient privacy concerns.

In this article, we present a novel deep-learning-based computational framework based on our preliminary work [2] to solve the undersampled inverse problems with convergence guarantee, tackling the aforementioned issues. We focus on medical image reconstruction applications, particularly SVCT reconstruction, to demonstrate our main ideas. Our framework can be applied to reconstruction problems with more than one domain, such as dual-domain SVCT reconstruction, and it naturally connects the domains through the physics of the image formation process and integrates a data-driven strategy from deep learning into the variational method in classical mathematical imaging. This results in a *parameterized* objective function, which can learn higher level features in both domains, possibly non-convex and non-smooth. Then, we develop a novel learned alternating minimization algorithm (LAMA) to optimize this objective function. The parameterized regularizers on both image and measurement domains are then trained recursively, while the network parameters are shared across iterations to ensure memory efficiency and maintain the integrity of the optimization algorithm.

Our approach leads to a novel deep network architecture following the exact derived optimization algorithm. This allows the network to inherit all the convergence properties of the algorithm, thereby enhancing the interpretability of our architecture by minimizing a regularized energy function. Our experimental results, combined with convergence analysis, demonstrate the **efficacy, stability, and interpretability** of our method.

## II. RELATED WORK

Computed Tomography (CT) stands as one of the foremost medical imaging technologies widely employed in clinical settings. Utilizing X-ray emissions, CT scanners calculate the X-ray attenuation across various tissues within the human body from differing angles. Sparse-view CT, a variant of traditional CT imaging, notably diminishes the number of scan angles, thereby significantly reducing the volume of sinogram data obtained. This reduction aims to mitigate the potential adverse effects of X-ray radiation on patients. Nevertheless, the reconstruction of the original image from such sparsely sampled CT data poses a formidable challenge, given its severely underdetermined nature [3]–[7]. Consequently, an adept reconstruction methodology is imperative to derive high-fidelity images from sparse-view data. Variational methods emerge as a robust mathematical framework that addresses a

Yunmei Chen is a Distinguished Professor with the Department of Mathematics, University of Florida, Gainesville, FL 32611 (email: yun@ufl.edu). Chi Ding and Qingchao Zhang are with the Department of Mathematics, University of Florida, Gainesville, FL 32611 (email: ding.chi@ufl.edu, qingchaozhang3@gmail.com).

Ge Wang is Clark & Crossan Chair Professor and director of the Biomedical Imaging Center, Rensselaer Polytechnic Institute, Troy, NY 12180 (email: wangg6@rpi.edu).

Xiaojing Ye is a professor at the Department of Mathematics & Statistics, Georgia State University, Atlanta, GA 30302 (email: xye@gsu.edu).

(Corresponding author: Yunmei Chen)

broad spectrum of image reconstruction challenges. Typically, these methods reframe image reconstruction as an energy minimization task, wherein the objective function comprises a data fidelity term—reflecting the disparity between the acquired data and the target image—and a regularization term, which encodes prior knowledge or desired image characteristics. While the data fidelity term is dictated by the underlying physics of the imaging process, the regularization term often assumes relatively simple forms, such as the squared  $L^2$  norm of image gradients or the total variation of images.

Variational methods offer remarkable versatility and adaptability, accommodating diverse imaging modalities and effectively handling varying degrees of data sparsity to enhance the quality of reconstructed images. Despite numerous theoretical advancements and promising empirical outcomes, the manually crafted regularization employed in conventional variational methods often falls short in capturing intricate image structures, thereby constraining reconstruction quality. Moreover, the optimization of objective functions, particularly those non-convex and non-smooth in nature, necessitates extensive iterations, leading to slow convergence rates and prolonged computational times in real-world applications.

#### A. Deep learning in CT image reconstruction

In recent years, deep learning (DL) has emerged as a powerful tool for image reconstruction. At the heart of DL is deep neural networks (DNNs), which are a class of nonlinear parametric functions that can approximate highly complicated functions with high accuracy [8]–[10]. In practice, DL-based methods use DNNs as surrogates of the functions of interest and learn the parameters of these DNNs using training data. The generalized data-driven learning framework enables DL to learn powerful high-level features from data for the target task. Thus, DL has produced promising empirical results in various applications.

Unrolling deep networks [11]–[15] have become a major type of network architecture for image reconstruction. An unrolling network picks some iterative optimization scheme and mimics the latter by treating one iteration as one layer of the network, i.e., the structure of the layer follows the computations in the iteration. But certain term(s) in that iteration, e.g., the proximal mapping, is replaced by a neural network with trainable parameters. The output of the unrolling network is set to be the result after a prescribed number of iterations (layers), and the parameters are trained by minimizing the error of the output to the ground truth image. The name “unrolling” thus refers to unfolding the iterative optimization scheme to form such an end-to-end network. Optimization algorithms leveraging information in image domain [13], [16]–[20], sinogram (data) domain [21]–[23], and both domains [14], [24]–[26] have been proposed. Among these methods, dual-domain-based networks have been shown to outperform the others due to the advantage of adaptive feature selection and dynamic interactions in both domains [24], [25]. Therefore, alternating minimization (AM), also known as block coordinate descent (BCD), and similar algorithms become natural choices for reconstruction problems

involving two domains. These algorithms are also designed to tackle optimization problems with two variables.

#### B. Alternating Minimization and related unrolling networks

AM and alike, including the Alternating Direction Method of Multipliers (ADMM) in a broad sense, have been well studied in the optimization literature, but mainly in the context of convex problems, where the objective functions are convex. For non-convex problems, the proximal alternating linearized minimization (PALM) algorithm [27] is developed where the algorithm alternates between the steps of the proximal forward-backward scheme. A follow-up work [28] proposed an inertial version of the PALM (iPALM) algorithm motivated by the Heavy Ball method of Polyak [29]. It is also closely related to multi-step algorithms of Nesterov’s accelerated gradient method [30]. The global convergence to a critical point is obtained for PALM and iPALM relying on the Kurdyka-Łojasiewicz (KL) property. In addition, these two algorithms assume the joint term for two blocks to be smooth (possibly nonconvex), and the proximal points associated with these terms are trivial to obtain.

Numerous unrolling networks inspired by AM optimization algorithms have been proposed recently. Prominent examples include ADMM-Net [31], Deeply Aggregated Alternating Minimization Neural Network (DeepAM) [32], and BCD-Net [33], among others. These frameworks signify a convergence between traditional optimization methodologies and contemporary deep learning paradigms, demonstrating their potential for advancing image reconstruction tasks.

#### C. Convergence and stability of unrolling networks

Despite numerous empirical successes, unrolling methods raise major concerns. These methods only superficially mimic existing iterative optimization schemes but lose the theoretical integrity of the regularization model. They do not correspond to any specified objective function and, thus, do not possess any theoretical justifications or convergence guarantees under any specific optimality. In recent years, there has been a surge of interest in constructing convergent unrolling networks [34]. There are mainly two types of network convergence considered in the literature: convergence in objective function value [15] and in fixed-point iteration (FPI) [35]–[38]. Convergence of FPI leverages a fixed-point mapping parameterized as a deep network whose parameters  $\theta$  can be learned from data. Convergence can be established as long as the neural network’s spectral radius falls in  $[0, 1)$  for any input imaging data, ensuring convergence due to the network’s non-expansiveness. However, such an assumption may result in a large spectral radius and, thus, slow convergence in some medical imaging. In a specific class of FPI networks, training requires solving FPI and inverting operators using the Neumann series, which can be slow and unstable. Moreover, FPI networks do not link the limit points to any objective function, making it difficult to interpret the optimality of the solutions as in traditional variational methods in mathematical imaging.

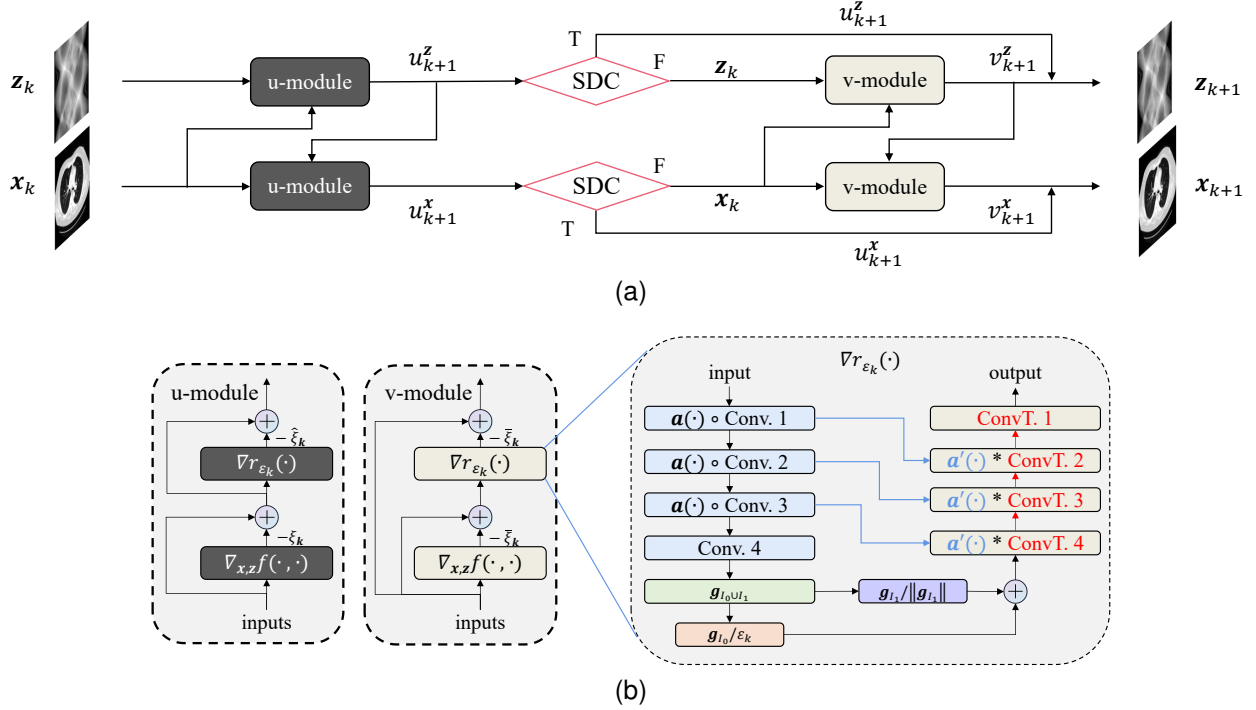


Figure 1. Structure of one LAMA phase. (a) Schematic illustration of one phase in LAMA, where u-module employs residual learning architecture and v-module safeguards convergence. The  $k$ th phase has  $(\mathbf{x}_k, \mathbf{z}_k)$  as input and  $(\mathbf{x}_{k+1}, \mathbf{z}_{k+1})$  as output. LAMA is constructed by  $K$  such phases. (b) Structures of the u-module, v-module, and the unrolling of the gradient over smoothed regularization operator  $\nabla r_{\varepsilon_k}$  defined in equation (13). Note that  $\xi$  denotes either  $\alpha$  or  $\beta$ .  $f$  is the data fidelity and data consistency function defined in equation (7) while  $\nabla_{\mathbf{x}, \mathbf{z}} f$  denote the gradient of  $f$  w.r.t. either  $\mathbf{x}$  or  $\mathbf{z}$ . Conv.  $i$  and ConvT.  $i$  denote the convolutional layer and convolution transpose with weights of the  $i^{\text{th}}$  corresponding instance, respectively.  $a(\cdot)$  is the smoothed activation function, and  $a'(\cdot)$  is the derivative of  $a(\cdot)$ . The unrolling of  $\nabla r_{\varepsilon_k}$  into a neural network that exactly follows the mathematical formulation.

### III. METHODOLOGY

This section presents the reconstruction pipeline for solving the SVCT reconstruction problem. It starts with an initialization network, which is a recursive predictive network that learns an interpolation mechanism that inputs the sparse-view data and generates an approximated full-view sinogram. This output is then provided to the reconstruction model, where we apply the standard filtered back-projection (FBP) to obtain a higher-quality image as the initial input. The reconstruction network is unrolled by an interpretable variational model and the induced convergent alternating minimization algorithm.

#### A. Recurrent Initialization Network

First, we propose a simple but highly effective recurrent initialization network to generate adequate initial images for sparse-view CT reconstruction. We will show that such initial images substantially improve our method's efficiency and accuracy.

We denote  $\mathbf{s}$ , the full-view sinogram data of an image  $\mathbf{x}$ , and  $\mathbf{s}_0$ , the sparse-view data acquired during the scan. Suppose  $\mathbf{A}$  is the discrete Radon transform and  $\mathbf{P}_0$  is the binary matrix representing the selection of the sparse-view data  $\mathbf{s}_0$ , then we have:

$$\mathbf{s} = \mathbf{A}\mathbf{x} \quad \text{and} \quad \mathbf{P}_0\mathbf{s} = \mathbf{P}_0\mathbf{A}\mathbf{x} = \mathbf{s}_0. \quad (1)$$

Recall that the core technique here is to build a deep neural network  $\bar{\Psi}_\theta$  with parameter denoted by  $\theta$ , such that it can map any sparse-view tomographic data  $\mathbf{s}_0$  to a refined

sinogram  $\bar{\Psi}_\theta(\mathbf{s}_0)$  close to the corresponding ground truth  $\mathbf{s}^*$ . The parameter  $\theta$  is learned by minimizing the mean squared error between  $\bar{\Psi}_\theta(\mathbf{s}_0)$  and  $\mathbf{s}^*$ , averaged over the training dataset of a sufficient amount of such image-vs-data pairs  $(\mathbf{s}^*, \mathbf{s}_0)$ , like in standard supervised learning.

Suppose the sparse-view scan only acquires  $1/p$  of the full-view data, where  $p \in \mathbb{N}$  is the downsampling rate, then the full-view sinogram  $\mathbf{s}$  can be rearranged into  $\mathbf{s} = [\mathbf{s}_0, \mathbf{s}_1, \dots, \mathbf{s}_{p-1}]$ . Here the sparse-view sinogram data  $\mathbf{s}_0 = [\mathbf{s}_0^1, \dots, \mathbf{s}_0^V]$  contains a total of  $V$  views, and  $\mathbf{s}_0^j$  is the measurement vector obtained by the detector at angle  $\vartheta_{jp}$  for partitions indexed by  $j = 1, \dots, V$ . See Fig. 2 for demonstration using  $p = 4$ , where  $\Delta\vartheta = \vartheta_1 - \vartheta_0$  is the angle between two adjacent angles in a full-view sinogram. Let  $\mathbf{P}_i$  be the selection matrix corresponding to  $\mathbf{s}_i$ , i.e.,  $\mathbf{P}_i\mathbf{s} = \mathbf{s}_i$ , for  $i = 1, \dots, p$ . Then we have the following relation between  $\mathbf{s}_0$  and  $\mathbf{s}_1$ :

$$\mathbf{s}_1 = \mathbf{P}_1\mathbf{s} = \mathbf{P}_1\mathbf{A}\mathbf{x} \approx \mathbf{P}_1\mathbf{A}\bar{\Psi}_\theta(\mathbf{s}_0) = \bar{\Psi}_\theta(\mathbf{s}_0), \quad (2)$$

where  $\bar{\Psi}_\theta := \mathbf{P}_1\mathbf{A}\bar{\Psi}_\theta$ . Then  $\bar{\Psi}_\theta$  is essentially the mapping from  $\mathbf{s}_0$  to  $\mathbf{s}_1$  based on the reconstruction network  $\bar{\Psi}_\theta$ . Therefore, we can also use some neural network  $\bar{\Psi}_\theta$  to directly approximate the mapping from  $\mathbf{s}_0$  to  $\mathbf{s}_1$ .

On the other hand, if the CT scanner samples at the angle  $\vartheta_1$  rather than  $\vartheta_0$  in Fig. 2, then  $\mathbf{s}_1$  is obtained instead. This is equivalent to using the same scan pattern in Fig. 2 but with the subject  $\mathbf{x}$  rotated clockwise for angle  $\Delta\vartheta$ . As such, we can see that  $\mathbf{s}_2 = \bar{\Psi}_\theta(\mathbf{s}_1)$  due to equation (2) because  $\mathbf{s}_2$  to  $\mathbf{s}_1$  is as  $\mathbf{s}_1$  to  $\mathbf{s}_0$  now. In other words,  $\bar{\Psi}_\theta$  approximates the mapping from a sparse-view data to another rotated counterclockwise for

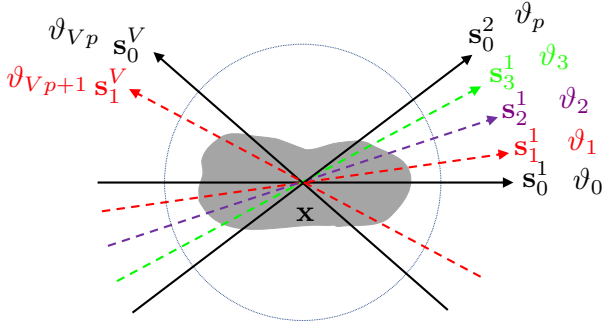


Figure 2. Demonstration of recursive relations between measurement data  $\mathbf{s}$  and view angles  $\vartheta$ . The gray area indicates the subject  $\mathbf{x}$ . Solid black arrows show the angles that are actually acquired in the sparse-view CT scan, and dash red/purple/green arrows show the skipped views. Here  $\mathbf{s} = [\mathbf{s}_0, \dots, \mathbf{s}_{p-1}]$  is the full-view data for  $p = 4$ ,  $\mathbf{s}_0 = [\mathbf{s}_0^1, \dots, \mathbf{s}_0^V]$  is the sparse-view data containing the measurement vectors at a total of  $V$  views, and  $\mathbf{s}_0^j$  is the measurement vector obtained by the detector at angle  $\vartheta_{jp}$  for partitions  $j = 1, \dots, V$ .

$\Delta\vartheta$ . To summarize, we expect to have the following recurrent relation hold approximately:

$$\mathbf{s}_0 \xrightarrow{\Psi_\theta} \mathbf{s}_1 \xrightarrow{\Psi_\theta} \dots \xrightarrow{\Psi_\theta} \mathbf{s}_{p-1} \xrightarrow{\Psi_\theta} \mathbf{s}_0^\dagger \quad (3)$$

where we omit subscripts as the refinement process is restricted within one partition, and  $\mathbf{s}_0^\dagger$  denotes the first sampling angle of the next partition. Therefore, we first construct a CNN  $\Psi_\theta$  in the sinogram domain, which is trained by solving

$$\min_{\theta} (1/pN) \cdot \sum_{n=1}^N \sum_{i=1}^p \|\Psi_\theta(\mathbf{s}_{i-1}^{(n)}) - \mathbf{s}_i^{(n)}\|^2 \quad (4)$$

with  $\mathbf{s}_p^{(n)} := \mathbf{s}_0^{(n+1)}$  for the  $n$ th full-view sinogram  $\mathbf{s}^{(n)}$  in the training dataset  $\{\mathbf{s}^{(n)} : n \in [N]\}$ .

Then we propose to our initialization network  $I_\theta$  defined as

$$I_\theta(\mathbf{s}_0) = \text{FBP}([\mathbf{s}_0, \Psi_\theta(\mathbf{s}_0), \dots, \Psi_\theta^{p-1}(\mathbf{s}_0)]) \quad (5)$$

where  $\Psi_\theta^i$  stands for the composition of  $\Psi_\theta$  for  $i$  times, and FBP is the standard filtered back-projection. In other words, we use  $\Psi_\theta$  to interpolate a full sinogram  $[\mathbf{s}_0, \Psi_\theta(\mathbf{s}_0), \dots, \Psi_\theta^{p-1}(\mathbf{s}_0)]$ , and use its FBP as the initial image for reconstruction.

### B. Learnable variational model

We formulate the variational reconstruction model as an AM problem, which is defined as follows:

$$\arg \min_{\mathbf{x}, \mathbf{z}} \Phi(\mathbf{x}, \mathbf{z}; \mathbf{s}, \Theta) := f(\mathbf{x}, \mathbf{z}; \mathbf{s}) + R(\mathbf{x}; \theta_1) + Q(\mathbf{z}; \theta_2) \quad (6)$$

where the physics for SVCT is modeled by

$$f(\mathbf{x}, \mathbf{z}) = \frac{1}{2} \|\mathbf{A}\mathbf{x} - \mathbf{z}\|^2 + \frac{\lambda}{2} \|\mathbf{P}_0\mathbf{z} - \mathbf{s}\|^2. \quad (7)$$

where  $\mathbf{s}$  stands for the available sparse-view sinogram for SVCT. The learnable parameters in our reconstruction model are denoted by  $\Theta = (\theta_1, \theta_2)$ . The model consists of data fidelity and consistency, which are captured by the function  $f(\mathbf{x}, \mathbf{z}; \mathbf{s})$ . The first part enforces the Radon transform of the image to be sufficiently close to the full-view sinogram  $\mathbf{z}$ ,

while the second part ensures the consistency of the down-sampled sinogram  $\mathbf{P}\mathbf{z}$  with the sparse-view sinogram ground truth. In this context,  $\mathbf{x}$  and  $\mathbf{z}$  represent the image and sinogram to be reconstructed, while  $\mathbf{A}$  is the Radon transform matrix. Additionally, we use learnable regularizations  $R(\mathbf{x}; \theta_1)$  and  $Q(\mathbf{z}; \theta_2)$  to help constrain the reconstruction. For simplicity, we omit any mention of learnable parameters and constants and rewrite the problem in equation (6) as follows:

$$\arg \min_{\mathbf{x}, \mathbf{z}} \Phi(\mathbf{x}, \mathbf{z}) := f(\mathbf{x}, \mathbf{z}) + R(\mathbf{x}) + Q(\mathbf{z}) \quad (8)$$

To impose sparsity on variations of data in the feature spaces, we adopt the  $L_{2,1}$  norm of learned features  $\mathbf{g}^R(\mathbf{x})$  and  $\mathbf{g}^Q(\mathbf{z})$  in the following as our regularizations:

$$R(\mathbf{x}) = \|\mathbf{g}^R(\mathbf{x})\|_{2,1} := \sum_{i=1}^{m_R} \|\mathbf{g}_i^R(\mathbf{x})\| \quad (9a)$$

$$Q(\mathbf{z}) = \|\mathbf{g}^Q(\mathbf{z})\|_{2,1} := \sum_{j=1}^{m_Q} \|\mathbf{g}_j^Q(\mathbf{z})\| \quad (9b)$$

Let  $r \in \{R, Q\}$ , we have  $\mathbf{g}^r(\cdot) \in \mathbb{R}^{m_r \times d_r}$ , where  $d_r$  is the number of channels, and each channel is a feature map with size  $\sqrt{m_r} \times \sqrt{m_r}$ . Note  $\mathbf{g}_i^r(\cdot) \in \mathbb{R}^{d_r}$  is the vector at position  $i$  across all channels. We apply the Vanilla CNN as the feature extractor  $\mathbf{g}^r(\cdot)$ :

$$\mathbf{g}^r(\mathbf{y}) = \mathbf{w}_l * a \cdots a(\mathbf{w}_2 * a(\mathbf{w}_1 * \mathbf{y})) \quad (10)$$

where  $\mathbf{w}_i$  denotes the convolution parameters for each layer,  $a(\cdot)$  is the smoothed ReLU activation function, and  $\mathbf{y}$  is the general input.

### C. The Learned Alternating Minimization Algorithm

We formally introduce the Learned Alternating Minimization Algorithm (LAMA) to solve the nonconvex and nonsmooth minimization model in equation (6). LAMA incorporates the residual learning architecture [39] to improve the practical learning performance by avoiding gradient vanishing in the training process with convergence guarantees. The algorithm consists of three stages, as follows:

The first stage of LAMA aims to reduce the nonconvex and nonsmooth problem in equation (6) to a nonconvex smooth optimization problem by using an appropriate smoothing procedure [15], [40]:

$$r_\varepsilon(\mathbf{y}) = \sum_{i \in I_0^r} \frac{1}{2\varepsilon} \|\mathbf{g}_i^r(\mathbf{y})\|^2 + \sum_{i \in I_1^r} \left( \|\mathbf{g}_i^r(\mathbf{y})\| - \frac{\varepsilon}{2} \right), \quad (11)$$

$$\mathbf{y} \in Y =: m_r \times d_r,$$

where  $(r, \mathbf{y})$  represents either  $(R, \mathbf{x})$  or  $(Q, \mathbf{z})$  and

$$I_0^r = \{i \in [m_r] \mid \|\mathbf{g}_i^r(\mathbf{y})\| \leq \varepsilon\}, \quad I_1^r = [m_r] \setminus I_0^r. \quad (12)$$

It is easy to show:

$$\nabla r_\varepsilon(\mathbf{y}) = \sum_{i \in I_0^r} \nabla \mathbf{g}_i^r(\mathbf{y})^\top \frac{\mathbf{g}_i^r(\mathbf{y})}{\varepsilon} + \sum_{i \in I_1^r} \nabla \mathbf{g}_i^r(\mathbf{y})^\top \frac{\mathbf{g}_i^r(\mathbf{y})}{\|\mathbf{g}_i^r(\mathbf{y})\|}, \quad (13)$$

$$\mathbf{y} \in Y =: m_r \times d_r,$$

The second stage solves the smoothed nonconvex problem with the fixed smoothing factor  $\varepsilon = \varepsilon_k$ , i.e.

$$\min_{\mathbf{x}, \mathbf{z}} \{\Phi_\varepsilon(\mathbf{x}, \mathbf{z}) := f(\mathbf{x}, \mathbf{z}) + R_\varepsilon(\mathbf{x}) + Q_\varepsilon(\mathbf{z})\}. \quad (14)$$



In light of the substantial improvement in practical performance by ResNet [39], we propose an inexact proximal alternating linearized minimization algorithm (PALM) [27] for solving equation (14). With  $\varepsilon = \varepsilon_k > 0$ , the scheme of PALM [27] is provided by:

$$\mathbf{b}_{k+1} = \mathbf{z}_k - \alpha_k \nabla_{\mathbf{z}} f(\mathbf{x}_k, \mathbf{z}_k) \quad (15a)$$

$$\mathbf{u}_{k+1}^{\mathbf{z}} = \arg \min_{\mathbf{u}} \frac{1}{2\alpha_k} \|\mathbf{u} - \mathbf{b}_{k+1}\|^2 + Q_{\varepsilon_k}(\mathbf{u}) \quad (15b)$$

and

$$\mathbf{c}_{k+1} = \mathbf{x}_k - \beta_k \nabla_{\mathbf{x}} f(\mathbf{x}_k, \mathbf{u}_{k+1}^{\mathbf{z}}) \quad (16a)$$

$$\mathbf{u}_{k+1}^{\mathbf{x}} = \arg \min_{\mathbf{u}} \frac{1}{2\beta_k} \|\mathbf{u} - \mathbf{c}_{k+1}\|^2 + R_{\varepsilon_k}(\mathbf{u}) \quad (16b)$$

where  $\alpha_k$  and  $\beta_k$  are step sizes. Since the proximal point  $\mathbf{u}_{k+1}^{\mathbf{x}}$  and  $\mathbf{u}_{k+1}^{\mathbf{z}}$  are difficult to compute, we approximate  $Q_{\varepsilon_k}(\mathbf{u})$  and  $R_{\varepsilon_k}(\mathbf{u})$  by their linear approximations at  $\mathbf{b}_{k+1}$  and  $\mathbf{c}_{k+1}$ , i.e.  $Q_{\varepsilon_k}(\mathbf{b}_{k+1}) + \langle \nabla Q_{\varepsilon_k}(\mathbf{b}_{k+1}), \mathbf{u} - \mathbf{b}_{k+1} \rangle$  and  $R_{\varepsilon_k}(\mathbf{c}_{k+1}) + \langle \nabla R_{\varepsilon_k}(\mathbf{c}_{k+1}), \mathbf{u} - \mathbf{c}_{k+1} \rangle$ , together with the proximal terms  $\frac{1}{2p_k} \|\mathbf{u} - \mathbf{b}_{k+1}\|^2$  and  $\frac{1}{2q_k} \|\mathbf{u} - \mathbf{c}_{k+1}\|^2$ . Then by a simple computation,  $\mathbf{u}_{k+1}^{\mathbf{x}}$  and  $\mathbf{u}_{k+1}^{\mathbf{z}}$  are now determined by the following formulas

$$\mathbf{u}_{k+1}^{\mathbf{z}} = \mathbf{b}_{k+1} - \hat{\alpha}_k \nabla Q_{\varepsilon_k}(\mathbf{b}_{k+1}), \quad (17a)$$

$$\mathbf{u}_{k+1}^{\mathbf{x}} = \mathbf{c}_{k+1} - \hat{\beta}_k \nabla R_{\varepsilon_k}(\mathbf{c}_{k+1}), \quad (17b)$$

where  $\hat{\alpha}_k = \frac{\alpha_k p_k}{\alpha_k + p_k}$ ,  $\hat{\beta}_k = \frac{\beta_k q_k}{\beta_k + q_k}$ . In deep learning approach, the step sizes  $\alpha_k$ ,  $\hat{\alpha}_k$ ,  $\beta_k$  and  $\hat{\beta}_k$  can also be learned. Note that the convergence of the sequence  $\{(\mathbf{u}_{k+1}^{\mathbf{z}}, \mathbf{u}_{k+1}^{\mathbf{x}})\}_k$  is not guaranteed. We proposed that if  $(\mathbf{u}_{k+1}^{\mathbf{z}}, \mathbf{u}_{k+1}^{\mathbf{x}})$  satisfy the following conditions:

$$\begin{aligned} \Phi_{\varepsilon_k}(\mathbf{u}_{k+1}^{\mathbf{x}}, \mathbf{u}_{k+1}^{\mathbf{z}}) - \Phi_{\varepsilon_k}(\mathbf{x}_k, \mathbf{z}_k) \leq \\ -\eta \left( \|\mathbf{u}_{k+1}^{\mathbf{x}} - \mathbf{x}_k\|^2 + \|\mathbf{u}_{k+1}^{\mathbf{z}} - \mathbf{z}_k\|^2 \right) \end{aligned} \quad (18a)$$

$$\|\nabla \Phi_{\varepsilon_k}(\mathbf{x}_k, \mathbf{z}_k)\| \leq \frac{1}{\eta} \left( \|\mathbf{u}_{k+1}^{\mathbf{x}} - \mathbf{x}_k\| + \|\mathbf{u}_{k+1}^{\mathbf{z}} - \mathbf{z}_k\| \right) \quad (18b)$$

for some  $\eta > 0$ , we accept  $\mathbf{x}_{k+1} = \mathbf{u}_{k+1}^{\mathbf{x}}$ ,  $\mathbf{z}_{k+1} = \mathbf{u}_{k+1}^{\mathbf{z}}$ . If any of (18a) and (18b) is violated, we compute  $(\mathbf{v}_{k+1}^{\mathbf{z}}, \mathbf{v}_{k+1}^{\mathbf{x}})$  by the standard AM (also called the Block Coordinate Descent algorithm, or BCD for short) with a simple line-search strategy to safeguard convergence: Let  $\bar{\alpha}, \bar{\beta}$  be positive numbers in  $(0, 1)$  compute

$$\mathbf{v}_{k+1}^{\mathbf{z}} = \mathbf{z}_k - \bar{\alpha} (\nabla_{\mathbf{z}} f(\mathbf{x}_k, \mathbf{z}_k) + \nabla Q_{\varepsilon_k}(\mathbf{z}_k)), \quad (19)$$

$$\mathbf{v}_{k+1}^{\mathbf{x}} = \mathbf{x}_k - \bar{\beta} (\nabla_{\mathbf{x}} f(\mathbf{x}_k, \mathbf{v}_{k+1}^{\mathbf{z}}) + \nabla R_{\varepsilon_k}(\mathbf{x}_k)). \quad (20)$$

Set  $\mathbf{x}_{k+1} = \mathbf{v}_{k+1}^{\mathbf{x}}$ ,  $\mathbf{z}_{k+1} = \mathbf{v}_{k+1}^{\mathbf{z}}$ , if for some  $\delta \in (0, 1)$ , the following holds:

$$\begin{aligned} \Phi_{\varepsilon}(\mathbf{v}_{k+1}^{\mathbf{x}}, \mathbf{v}_{k+1}^{\mathbf{z}}) - \Phi_{\varepsilon}(\mathbf{x}_k, \mathbf{z}_k) \leq \\ -\delta (\|\mathbf{v}_{k+1}^{\mathbf{x}} - \mathbf{x}_k\|^2 + \|\mathbf{v}_{k+1}^{\mathbf{z}} - \mathbf{z}_k\|^2). \end{aligned} \quad (21)$$

Otherwise we reduce  $(\bar{\alpha}, \bar{\beta}) \leftarrow \rho(\bar{\alpha}, \bar{\beta})$  where  $0 < \rho < 1$ , and recompute  $\mathbf{v}_{k+1}^{\mathbf{x}}, \mathbf{v}_{k+1}^{\mathbf{z}}$  until the condition in equation (21) holds.

The third stage checks if  $\|\nabla \Phi_{\varepsilon}\|$  has been reduced enough to perform the second stage with a reduced smoothing factor  $\varepsilon$ . By gradually decreasing  $\varepsilon$ , we obtain a subsequence of the iterates that converge to a Clarke stationary point (see Definition 1) of the original nonconvex and nonsmooth problem.

#### D. Architecture of LAMA Induced Neural Network

The architecture of the proposed multi-phase neural networks follows LAMA **EXACTLY** and is summarized in Fig. 1. Note that the convolution transpose and  $a'(\cdot)$  are direct consequences of the chain rule, demonstrating LAMA induced network follows exactly the iterative algorithm. Hence, we also use LAMA to denote the networks as each phase corresponds to each iteration. The networks inherit all the convergence properties of LAMA so that the solution is stabilized. Moreover, the algorithm effectively leverages complementary information through the inter-domain connections to accurately estimate the missing data. The network is also memory efficient due to parameter sharing across all phases. Since our alternating minimization algorithm adopts the parameters of the regularization term that is learnable from data, we call this method the Learned Alternating Minimization Algorithm (LAMA). A schematic plot of LAMA-Net is given in Fig. 1b, and the algorithm is summarized in the following:

---

**Algorithm 1** The Linearized Alternating Minimization Algorithm (LAMA)

---

**Input:** Initializations:  $\mathbf{x}_0, \mathbf{z}_0, \delta, \eta, \rho, \gamma, \varepsilon_0, \sigma, \lambda$

```

1: for  $k = 0, 1, 2, \dots$  do
2:    $\mathbf{b}_{k+1} = \mathbf{z}_k - \alpha_k \nabla_{\mathbf{z}} f(\mathbf{x}_k, \mathbf{z}_k)$ ,
3:    $\mathbf{u}_{k+1}^{\mathbf{z}} = \mathbf{b}_{k+1} - \hat{\alpha}_k \nabla Q_{\varepsilon_k}(\mathbf{b}_{k+1})$ 
4:    $\mathbf{c}_{k+1} = \mathbf{x}_k - \beta_k \nabla_{\mathbf{x}} f(\mathbf{x}_k, \mathbf{u}_{k+1}^{\mathbf{z}})$ 
5:    $\mathbf{u}_{k+1}^{\mathbf{x}} = \mathbf{c}_{k+1} - \hat{\beta}_k \nabla R_{\varepsilon_k}(\mathbf{c}_{k+1})$ 
6:   if (18) holds then
7:      $(\mathbf{x}_{k+1}, \mathbf{z}_{k+1}) \leftarrow (\mathbf{u}_{k+1}^{\mathbf{x}}, \mathbf{u}_{k+1}^{\mathbf{z}})$ 
8:   else
9:      $\mathbf{v}_{k+1}^{\mathbf{z}} = \mathbf{z}_k - \bar{\alpha} [\nabla_{\mathbf{z}} f(\mathbf{x}_k, \mathbf{z}_k) + \nabla Q_{\varepsilon_k}(\mathbf{z}_k)]$ 
10:     $\mathbf{v}_{k+1}^{\mathbf{x}} = \mathbf{x}_k - \bar{\beta} [\nabla_{\mathbf{x}} f(\mathbf{x}_k, \mathbf{v}_{k+1}^{\mathbf{z}}) + \nabla R_{\varepsilon_k}(\mathbf{x}_k)]$ 
11:    if (21) then  $(\mathbf{x}_{k+1}, \mathbf{z}_{k+1}) \leftarrow (\mathbf{v}_{k+1}^{\mathbf{x}}, \mathbf{v}_{k+1}^{\mathbf{z}})$  else
12:       $(\bar{\beta}, \bar{\alpha}) \leftarrow \rho(\bar{\beta}, \bar{\alpha})$  and go to 9
13:    end if
14:    if  $\|\nabla \Phi_{\varepsilon_k}(\mathbf{x}_{k+1}, \mathbf{z}_{k+1})\| < \sigma \gamma \varepsilon_k$  then  $\varepsilon_{k+1} = \gamma \varepsilon_k$  else
15:       $\varepsilon_{k+1} = \varepsilon_k$ 
16:    end for
17: return  $\mathbf{x}_{k+1}$ 

```

---

#### IV. CONVERGENCE ANALYSIS

Since the reconstruction is formulated as a nonconvex and nonsmooth optimization problem, we must introduce the following definitions based on the generalized derivatives.

Table I  
 QUANTITATIVE RESULTS (AAPM-MAYO) BY PSNR, SSIM, AND SINOGRAM RMSE WITH 64 AND 128 VIEWS. THE RMSE IS ON THE SCALE OF  $10^{-3}$ .  
 (TOP ONE HIGHLIGHTED)

Methods	64			128		
	PSNR	SSIM	RMSE ( $10^{-3}$ )	PSNR	SSIM	RMSE ( $10^{-3}$ )
FBP	27.17 ± 1.11	0.596 ± 9.0e-4	19.32 ± 6.04e-2	33.28 ± 0.85	0.759 ± 1.1e-3	6.88 ± 1.57e-4
DDNet [41]	35.70 ± 1.50	0.923 ± 3.9e-4	7.53 ± 1.96e-2	42.73 ± 1.08	0.974 ± 3.9e-5	3.29 ± 1.31e-3
LDA [15]	37.16 ± 1.33	0.932 ± 2.0e-4	3.31 ± 4.86e-4	43.00 ± 0.91	0.976 ± 1.9e-5	1.09 ± 7.26e-6
DuDoTrans [42]	37.90 ± 1.44	0.952 ± 1.0e-4	2.42 ± 5.94e-5	43.48 ± 1.04	0.985 ± 9.5e-6	0.97 ± 7.51e-6
LEARN++ [14]	43.02 ± 2.08	0.980 ± 3.2e-5	0.81 ± 2.43e-5	49.77 ± 0.96	0.995 ± 1.1e-6	0.31 ± 1.72e-6
LAMA (Ours)	44.58 ± 1.15	0.986 ± 7.1e-6	0.68 ± 9.97e-6	50.01 ± 0.69	0.995 ± 6.0e-7	0.32 ± 1.66e-6
initNet + LAMA (Ours)	<b>46.37 ± 0.99</b>	<b>0.990 ± 3.7e-6</b>	<b>0.52 ± 4.68e-6</b>	<b>51.02 ± 0.63</b>	<b>0.996 ± 3.7e-7</b>	<b>0.27 ± 7.13e-7</b>

Table II  
 QUANTITATIVE RESULTS (NBIA) BY PSNR, SSIM, AND SINOGRAM RMSE WITH 64 AND 128 VIEWS. THE RMSE IS ON THE SCALE OF  $10^{-3}$ . (TOP ONE HIGHLIGHTED)

Methods	64			128		
	PSNR	SSIM	RMSE ( $10^{-3}$ )	PSNR	SSIM	RMSE ( $10^{-3}$ )
FBP	25.72 ± 1.93	0.592 ± 1.6e-3	29.02 ± 0.26	31.86 ± 1.27	0.743 ± 1.7e-3	7.51 ± 4.60e-3
DDNet [41]	35.59 ± 2.76	0.920 ± 2.7e-4	7.26 ± 2.68e-2	40.23 ± 1.98	0.961 ± 1.2e-4	1.45 ± 7.79e-5
LDA [15]	34.31 ± 2.20	0.896 ± 3.9e-4	6.43 ± 1.85e-3	40.26 ± 2.57	0.963 ± 1.3e-4	1.76 ± 6.93e-5
DuDoTrans [42]	35.53 ± 2.63	0.938 ± 2.4e-4	2.40 ± 2.63e-4	40.67 ± 2.84	0.976 ± 6.2e-5	1.06 ± 4.21e-5
LEARN++ [14]	38.53 ± 3.41	0.956 ± 2.3e-4	1.52 ± 1.13e-4	43.35 ± 4.02	0.983 ± 5.3e-5	0.73 ± 2.27e-5
LAMA (Ours)	41.40 ± 3.54	0.976 ± 8.1e-5	0.99 ± 3.54e-5	45.20 ± 4.23	0.988 ± 3.0e-5	0.55 ± 1.24e-5
InitNet + LAMA (Ours)	<b>42.11 ± 4.09</b>	<b>0.979 ± 7.5e-5</b>	<b>0.92 ± 1.79e-5</b>	<b>47.28 ± 5.13</b>	<b>0.992 ± 1.5e-5</b>	<b>0.44 ± 7.40e-6</b>

*Definition 1:* (Clarke subdifferential). Suppose that  $f : \mathbb{R}^n \times \mathbb{R}^m \rightarrow (-\infty, \infty]$  is locally Lipschitz. The Clarke subdifferential of  $f$  at  $(\mathbf{x}, \mathbf{z})$  is defined as

$$\begin{aligned} \partial^c f(\mathbf{x}, \mathbf{z}) &:= \{(w_1, w_2) \in \mathbb{R}^n \times \mathbb{R}^m \mid \langle w_1, v_1 \rangle + \langle w_2, v_2 \rangle \\ &\leq \limsup_{(z_1, z_2) \rightarrow (\mathbf{x}, \mathbf{z}), t \rightarrow 0_+} \frac{f(z_1 + tv_1, z_2 + tv_2) - f(z_1, z_2)}{t}, \\ &\forall (v_1, v_2) \in \mathbb{R}^n \times \mathbb{R}^m\}. \end{aligned}$$

where  $\langle w_1, v_1 \rangle$  stands for the inner product in  $\mathbb{R}^n$  and similarly for  $\langle w_2, v_2 \rangle$ .

*Definition 2:* (Clarke stationary point) For a locally Lipschitz function  $f$  defined as in Def 1, a point  $X = (\mathbf{x}, \mathbf{z}) \in \mathbb{R}^n \times \mathbb{R}^m$  is called a Clarke stationary point of  $f$ , if  $0 \in \partial f(X)$ .

We can have the following convergence result.

*Theorem 1:* Let  $\{Y_k = (\mathbf{x}_k, \mathbf{z}_k)\}$  be the sequence generated by the algorithm with arbitrary initial condition  $Y_0 = (\mathbf{x}_0, \mathbf{z}_0)$ , arbitrary  $\varepsilon_0 > 0$  and  $\varepsilon_{tol} = 0$ . Let  $\{\tilde{Y}_l\} =: (\mathbf{x}_{k_l+1}, \mathbf{z}_{k_l+1})$  be the subsequence, where the reduction criterion in the algorithm is met for  $k = k_l$  and  $l = 1, 2, \dots$ . Then  $\{\tilde{Y}_l\}$  has at least one accumulation point, and each accumulation point is a Clarke stationary point.

## V. NUMERICAL TESTS

We demonstrate the performance of the proposed method LAMA on dual-domain SVCT reconstruction. In this case, we use two well-recognized benchmark CT datasets: (i) the 2016 NIH-AAPM-Mayo (AAPM-Mayo) Clinic Low-Dose CT Grand Challenge dataset and (ii) the National Biomedical Imaging Archive (NBIA) dataset. More details of data and noise generation can be found below.

### A. Experiment Setup

Among the deep-learning-based methods for the comparison experiments, DDNet [41] and LDA [15] are single-domain methods, while DuDoTrans [42], Learn++ [14], and LAMA are dual-domain methods. Notably, except for DuDoTrans, dual-domain methods have proven necessary for SVCT reconstruction problems to break the performance bottleneck. This underscores the essence of leveraging both modalities effectively, particularly when dealing with undersampled data. On top of the effectiveness of the dual-domain methods, our proposed method also outperforms the rest by a wide margin, and the design of our regularization network architecture is simple and memory efficient, as shown in Table III and Fig. 1. This further reveals the importance of interpretability and optimization-inspired insights that we embed into the training process and the network architecture design, contributing to the best reconstruction performance.

Given that our variational formulation in (6) is nonsmooth and nonconvex, avoiding unwanted local minima necessitates initializing the parameters (image/sinogram, network parameters) close to the ground truths. To achieve this, we employ a multi-phase recursive training strategy. Initially, a shallow feed-forward CNN is trained as the initialization network, yielding the initial image and sinogram  $(\mathbf{x}_0, \mathbf{z}_0)$ . Subsequently,  $(\mathbf{x}_0, \mathbf{z}_0)$  serves as input to the LAMA, generating  $(\mathbf{x}_i, \mathbf{z}_i)$  ( $i=1, 2, 3$ ). Then, we train the parameters of the 3-phase LAMA by minimizing the loss between  $(\mathbf{x}_3, \mathbf{z}_3)$  and the ground truth, obtaining a set of trained network parameters, denoted by  $\Theta_3$ . This process iterates, with  $(\mathbf{x}_3, \mathbf{z}_3)$  as input to the LAMA for subsequent phases until the 15th phase, where no obvious improvement is observed.

We randomly select 500 and 200 image-sinogram pairs from

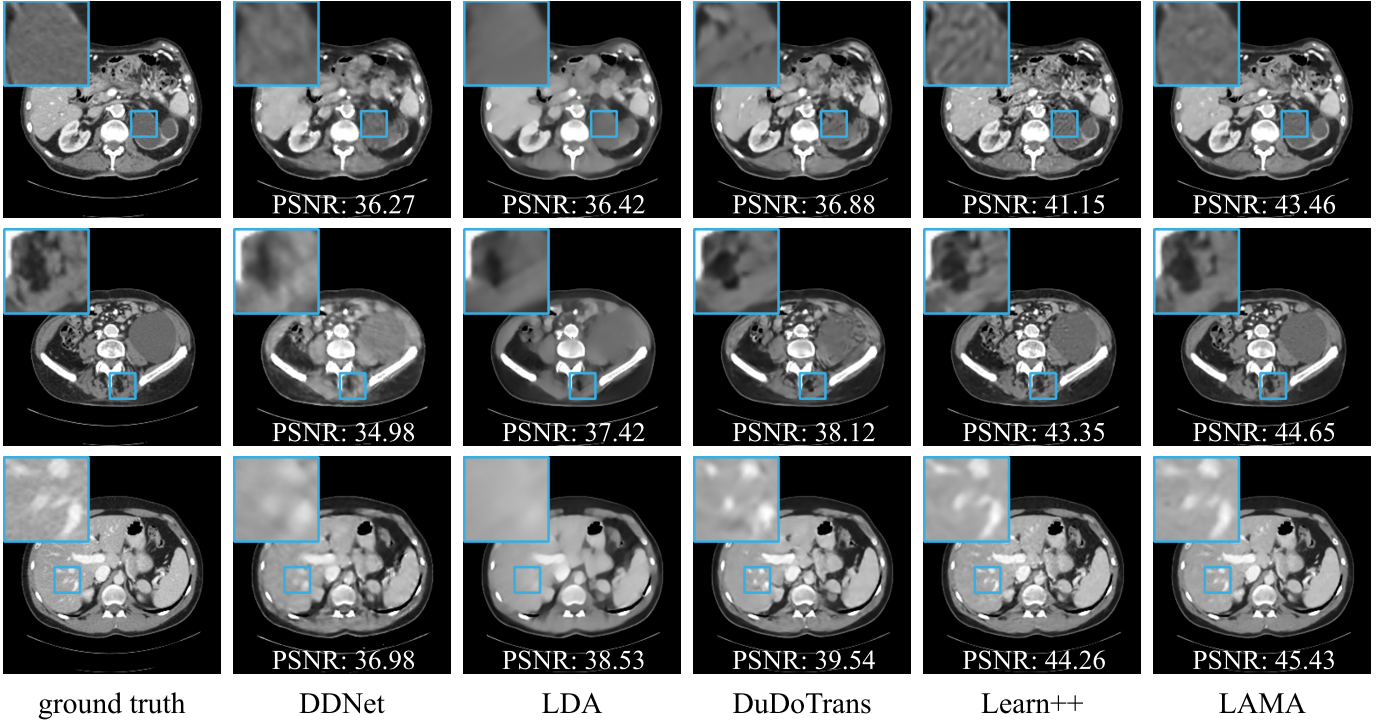


Figure 3. Visual comparison using 64-view siongrams for AAPM-Mayo dataset.

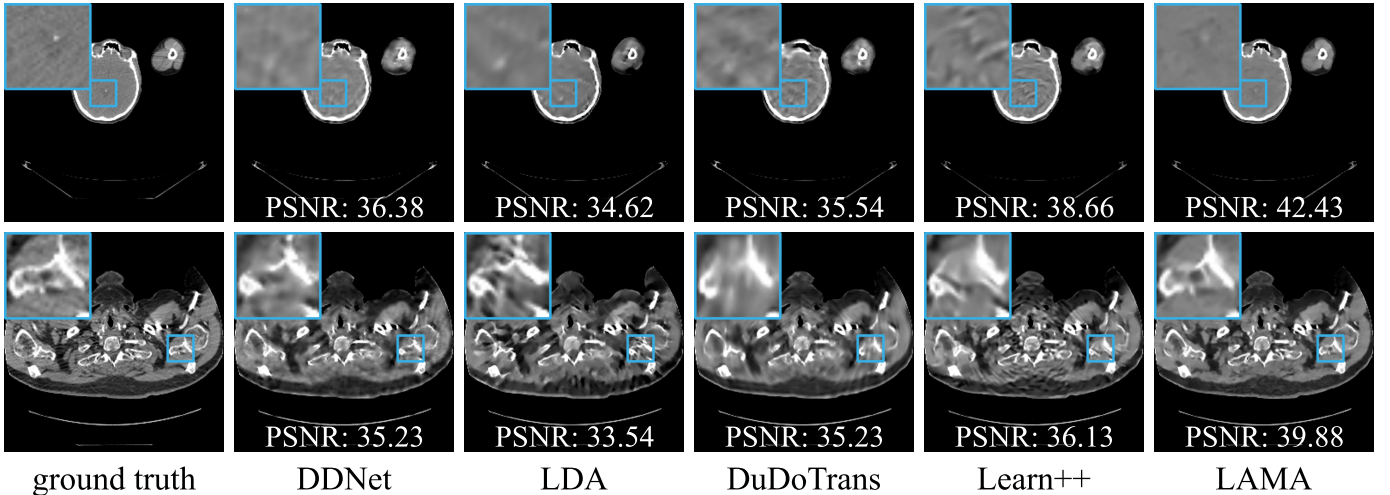


Figure 4. Visual comparison using 64-view siongrams for AAPM-NBIA dataset.

AAPM-Mayo and NBIA, respectively. In each dataset, we randomly split the data into two parts: 80% for training and 20% for testing. We call  $N$  the number of training data pairs. We evaluate algorithms using the peak signal-to-noise ratio (PSNR), structural similarity (SSIM) [43], and the number of parameters in all compared networks. The sinogram has 512 detector elements and 1024 evenly distributed full projection views.

In this SVCT experiment, the 1024 sinogram views are downsampled into 64 (6.25%) or 128 (12.5%) views to reduce the harmful X-ray dose to patients. The full image size is  $256 \times 256$ , and we simulate projections and back-projections

in fan-beam geometry using distance-driven algorithms [44] implemented in a PyTorch-based library CTLIB [45].

Given  $N$  training data pairs  $\{(s^{(i)}, \hat{x}^{(i)})\}_{i=1}^N$ , where  $s^{(i)}$  is sparse-view CT data and  $\hat{x}^{(i)}$  is the corresponding ground truth image, the loss function for training the regularization networks is defined as:

$$\mathcal{L}(\Theta) = \frac{1}{N} \sum_{i=1}^N \left\| \mathbf{x}_K^{(i)} - \hat{\mathbf{x}}^{(i)} \right\|^2 + \left\| \mathbf{z}_K^{(i)} - \mathbf{A} \hat{\mathbf{x}}^{(i)} \right\|^2 + \mu \left( 1 - \text{SSIM}(\mathbf{x}_K^{(i)}, \hat{\mathbf{x}}^{(i)}) \right), \quad (22)$$

where  $\mu$  is the weight for SSIM loss set as 0.01 for all ex-

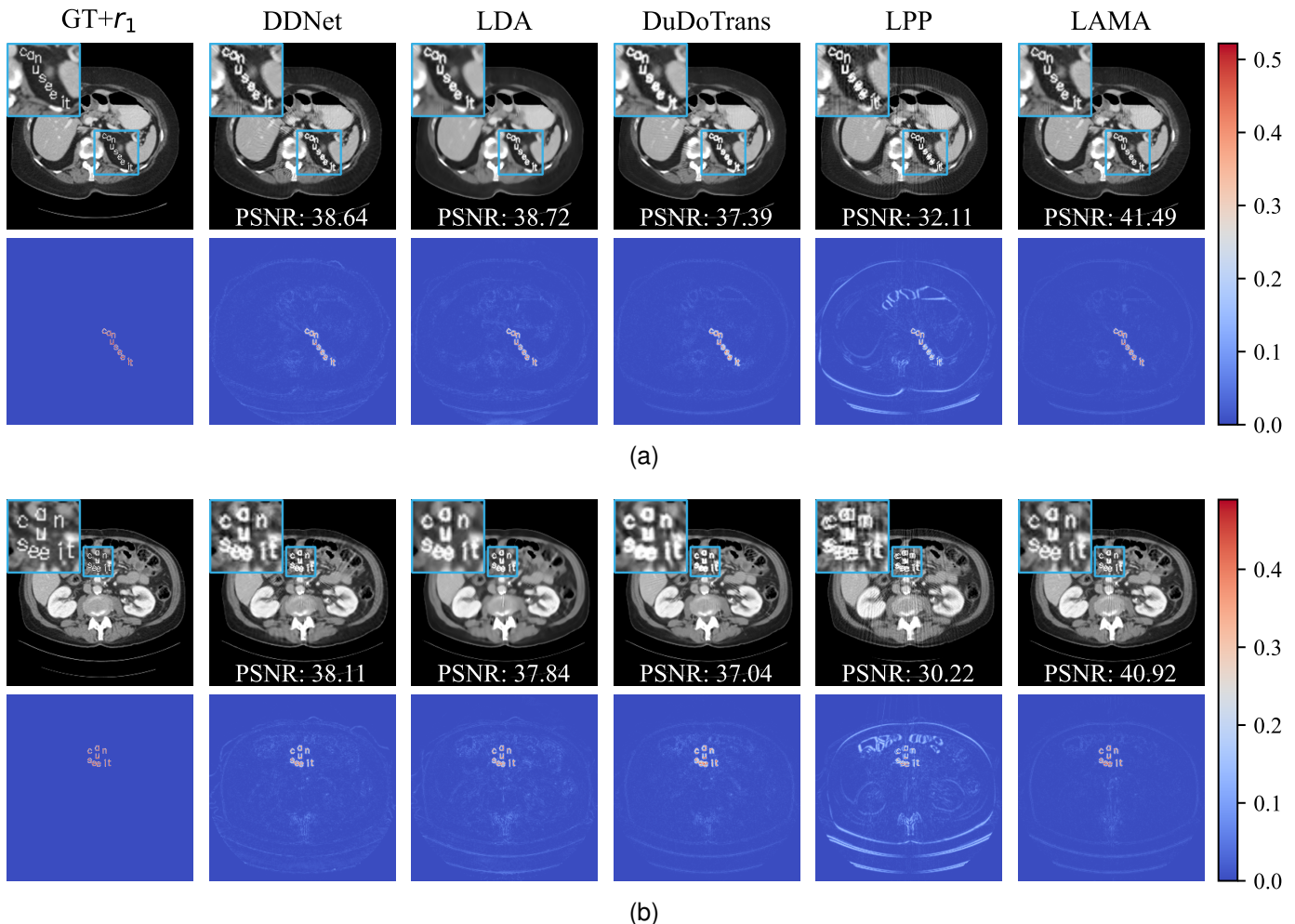


Figure 5. Two examples of different algorithms using input with structured perturbation  $r_1$ . The first rows are reconstructed images with zoomed-in perturbed areas in the top left corner and annotated PSNR between the reconstructed image and perturbed ground truth  $GT+r_1$ . The second rows are difference heat maps between the reconstructed images and the unperturbed ground truth.

periments, and  $(\mathbf{x}_K^{(i)}, \mathbf{z}_K^{(i)}) := \text{LAMA}(\mathbf{x}_0^{(i)} := \mathbf{A}^\top \mathbf{s}^{(i)}, \mathbf{z}_0^{(i)} := \mathbf{s}^{(i)})$  by applying LAMA for a prescribed  $K$  iterations ( $K$  set to 15 in our experiments).

We use the Adam optimizer with learning rates of  $1e-4$  and  $6e-5$  for the image and sinogram networks, respectively, and train them with the recursive approach. All the other parameters are set to the default of Adam [46]. The training starts with three phases for 300 epochs, then adding two phases for 200 epochs each time until the number of phases reaches 15. The algorithm is implemented in PyTorch-Python version 1.10. Our experiments were run on a Linux server with an 80G NVIDIA A100 Tensor Core GPU.

We show experimental results on two different testing setups using the two datasets above: The first test compares reconstruction quality directly to several state-of-the-art deep reconstruction networks, and the second test verifies LAMA’s excellent stability connected to its convergence property.

### B. Comparison in reconstruction quality

We evaluate LAMA by applying sparse-view sinograms and the images obtained by FBP from the test set. We test state-of-the-art methods: DDNet [41], LDA [15], DuDoTrans [42],

Table III  
NUMBER OF PARAMETERS FOR DIFFERENT METHODS. (TOP TWO HIGHLIGHTED)

Methods	initNet	DDNet	LDA	DuDoTrans	LEARN++	LAMA	InitNet+LAMA
# Parameters	1e5	6e5	<b>6e4</b>	8e6	6e6	<b>3e5</b>	4e5

Learn++ [14]. The reconstruction quality is evaluated using PSNR, SSIM, and sinogram RMSE, which are presented in Table I for the AAPM-Mayo and NIBIA datasets, respectively. Note that we provide sinogram RMSE to demonstrate the effectiveness of LAMA as a dual-domain method that leverages complementary information. Moreover, the network sizes of these compared networks are shown in III. Example reconstructed images (with zoom-ins) of these methods on the two datasets are shown in Fig. 3.

From Tables I and II, we can see LAMA performs favorably against the state-of-the-art deep reconstruction networks: it attained the highest PSNR and SSIM among all compared methods. These indicate that LAMA is highly accurate in image reconstruction after training on small-size datasets. LAMA also produces the least and the second least sinogram RMSE,



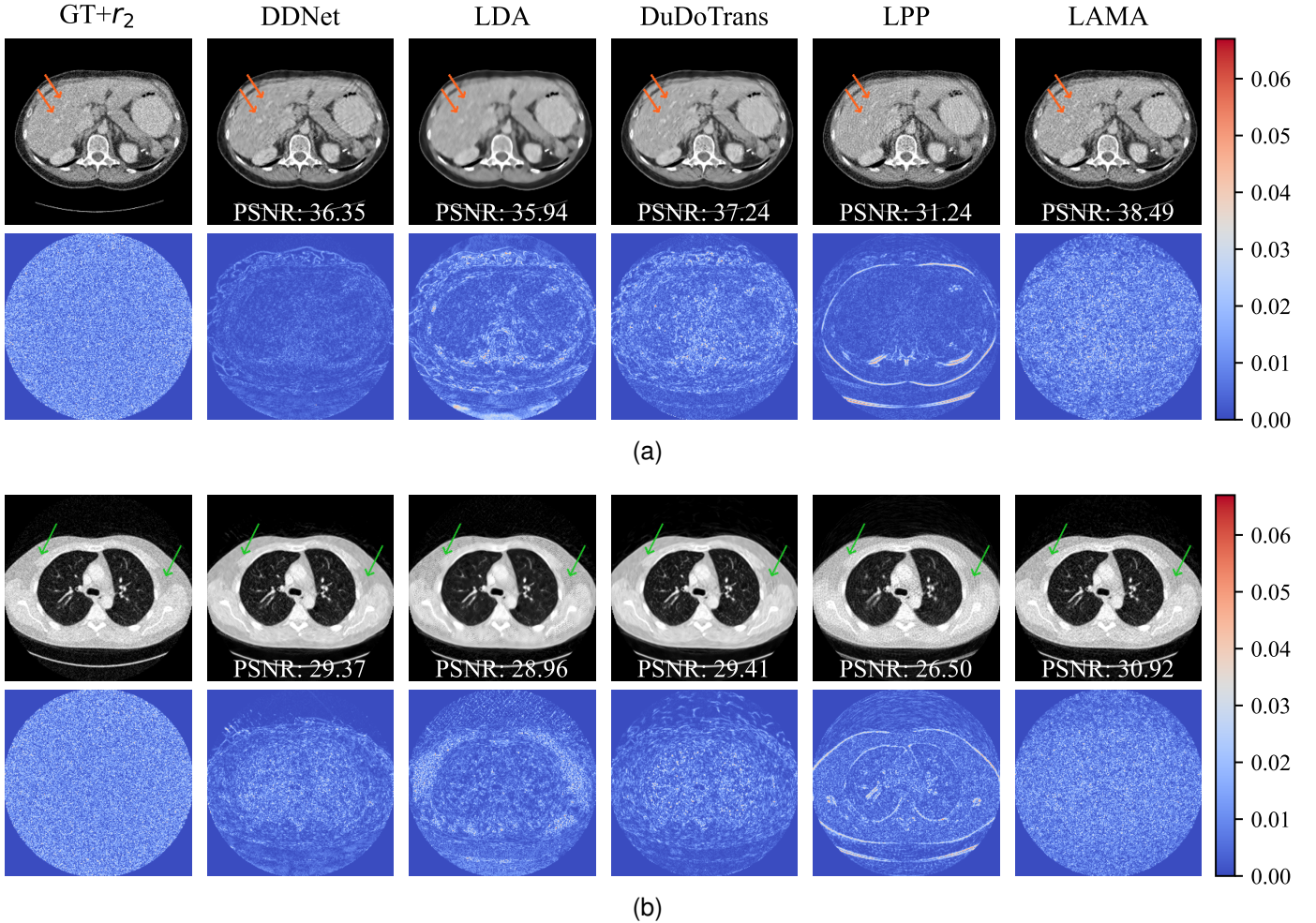


Figure 6. Example results of reconstructed images with annotated PSNR between the reconstructed image and the perturbed ground truth  $GT+r_2$ , where  $r_2$  is Gaussian noise. (a)  $r_2$  is zero mean with a standard deviation of 0.03. (b)  $r_2$  is zero mean with a standard deviation of 0.05.

proving that our method effectively exploits information from both domains. Notably, the subtle decrease in sinogram RMSE with increasingly accurate reconstruction yields substantial improvements in PSNR and SSIM metrics, highlighting the pivotal role of refinements in the observation data, namely, the sinogram. This observation not only underscores the efficacy of LAMA in recovering the original observation but also suggests a proximity to a globally optimum solution. Meanwhile, LAMA uses the second lowest number of parameters without the initial network in the list of compared networks. This demonstrates that LAMA is highly parameter-efficient compared to state-of-the-art deep reconstruction networks. Fig. 3 further demonstrates that LAMA can effectively preserve structural details in reconstructed images when removing noise and artifacts.

### C. Test on solution stability

In this test, we consider a widely concerned stability issue of deep neural networks. Specifically, we conduct a series of experiments to investigate the stability of LAMA heuristically, given that it is provably convergent as a strong indication of stability. For comparison purposes, we also show the results of the other state-of-the-art methods under the same

test environment. We follow the stability tests discussed in [47] and evaluate the compared methods under two types of perturbations: structured noise  $r_1$  and Gaussian noise  $r_2$ . These perturbations are applied to mimic typical sensor failures [47]. For the structured noise, we add the text “can you see it” to highly structured areas in the ground truth CT images and then apply the same physical process to generate SVCT data. For Gaussian noise, they are added to the entire ground truth images. Note that all compared methods, including LAMA, are trained with clean data without applying adversarial training strategies or the noises mentioned above. The results are shown in Fig. 5 and 6, respectively. These two figures show that LAMA recovers the ground truth much more faithfully than other methods under perturbations  $r_1$  and  $r_2$ .

Our method demonstrates a notable capability in handling the structured noise  $r_1$  “can u see it”. In Fig. 5, the preservation of  $r_1$  shows that LAMA can treat outliers independently without introducing additional artifacts or instabilities as  $LAMA(\mathbf{x}+r_1, \mathbf{z}+r_1) \approx LAMA(\mathbf{x}, \mathbf{z})+r_1$ , distinguishing it from alternative approaches. The difference map between the reconstructed images and the clean ground truth effectively illustrates the degree of perturbation present in the images beyond the effects of  $r_1$ . Notably, in both examples, our

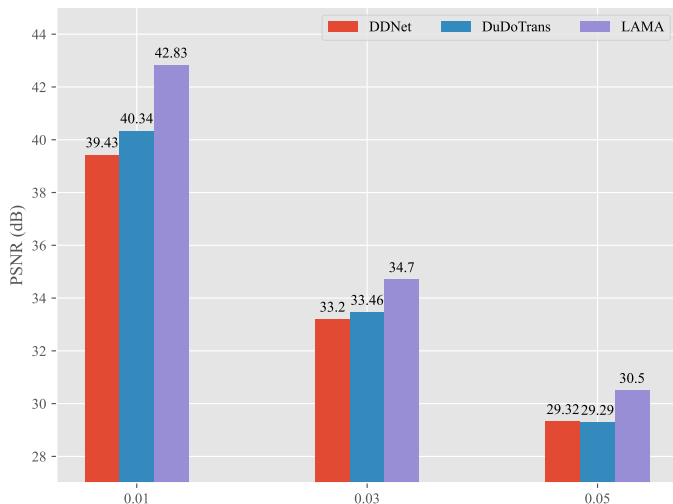


Figure 7. We pick the top-3 most stable algorithms (DDNet, DuDoTrans, LAMA) and compare their reconstruction PSNR with perturbed ground truth by different Gaussian noise levels with standard deviation 0.01, 0.03, and 0.05, respectively, where the image pixel range is normalized between 0 and 1.

approach, LAMA, exhibits the least detail loss compared to other methods. This is evidenced by the noticeable retention of information, particularly highlighted by contours or edges in the difference heatmap, which are clearly more apparent in other methods. Overall, other methods either show distortions not appearing in the original image or compromise small structures by over-smoothing. In contrast, fine structures are still clearly visible for our proposed method.

If the data is added with Gaussian noise  $r_2$ , note that in Fig. 6, both difference heatmaps in the first column are the standard disk of Gaussian noise  $r_2$  where no pattern or information related to the image can be observed. Notably, LAMA displays a similar behavior, indicating a relationship approximated by  $\text{LAMA}(\mathbf{x} + r_2, \mathbf{z} + r_2) \approx \text{LAMA}(\mathbf{x}, \mathbf{z}) + r_2$ . This characteristic is desirable as it signifies the algorithm’s stability in effectively isolating and distinguishing noise from the essential information during the reconstruction process. In contrast, other methods such as DDNet, LDA, and DuDoTrans either tend to compromise small structures in Fig. 6a or excessively smooth certain areas of the reconstructed images in Fig. 6b, particularly evident in the areas pointed by arrows. While this may enhance visual appeal, it poses a risk of information loss. This concern is further established by the difference heatmap, revealing substantial disparity in the form of clearly visible highlighted contours and sharp edges, indicative of potential loss of critical details. LAMA also consistently produces more stable reconstructions for different noise levels than other methods shown in Fig. 7.

The LAMA induces a deep neural network mirroring its architecture, significantly reducing network complexity and enhancing memory efficiency and reconstruction accuracy while inheriting the convergence property of the algorithm. This deep network approximates the variational model, incorporating learnable regularizers in both image and measurement domains, along with data fidelity and other constraints. Despite the potential for local minima due to the noncon-

vexity and nonsmoothness of the regularizers, our initial network and recursive training strategy keep the output close to the ground truth. Hence, our approach facilitates decent reconstruction even without adversarial training, as perturbed images/sinograms tend to exhibit sparsity under the same learned transformations/features from unperturbed data. This computational stability is evident in the faithfulness of features (mostly dark in the difference heatmap Fig. 8 (c) other than the perturbed area “can u see it”), indicating the effectiveness of regularizers learned from unperturbed data in handling perturbations, thereby affirming the stability of the LAMA.

Overall, the PSNR of reconstructed images corroborates the visual results, where LAMA consistently achieves superior reconstruction quality, demonstrating its stability under perturbation for both  $r_1$  and  $r_2$ .

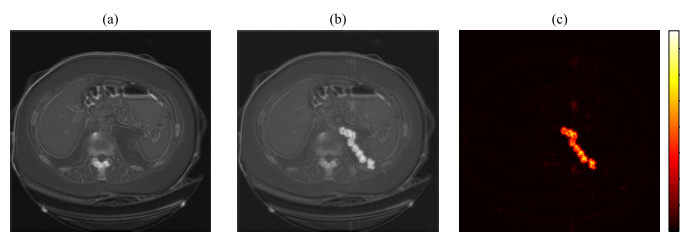


Figure 8. (a) The  $L^2$ -norm of  $g^R(\mathbf{x})$  ( $\|g^R(\mathbf{x})\|$ ), where the feature extractor  $g^R$  is defined in Eq. (9) and learned from clean training data. (b) The  $L^2$ -norm of  $g^R(\mathbf{x} + r_1)$  ( $\|g^R(\mathbf{x} + r_1)\|$ ), where  $r_1$  is the perturbation added on  $\mathbf{x}$ . (c) The difference heatmap between (a) and (b).

## VI. CONCLUSION

We propose a novel, interpretable, and stable dual-domain CT image reconstruction algorithm, LAMA. It is a generalization of the Learnable Descent Algorithm (LDA) [15] to the two-block case. Compared to LDA, which is based on a gradient descent scheme, the generalization introduced by LAMA requires a very different and more careful algorithmic design since alternating minimization is, in general, not convergent in a nonconvex setting. Moreover, we integrated a more adaptive descent condition in the design of LAMA so that the variable to safeguard convergence is only updated when the condition is met. In addition, unlike most alternating minimization schemes in the optimization literature, LAMA does not require the KL property for convergence—this enables the use of arbitrary Lipschitz continuous neural networks in the LAMA framework. Moreover, by introducing learnable regularizations, our method effectively suppresses noise and artifacts while preserving structural details in the reconstructed images. The LAMA algorithm leverages complementary information from both domains to estimate missing information and improve reconstruction quality in each iteration. Our experiments demonstrate that LAMA outperforms existing methods while maintaining favorable memory efficiency. By incorporating the recursive training strategy and the convergence property of our algorithm, it has also been heuristically proven to have outstanding stability compared with other methods, even without adversarial training or including perturbation in training data.



APPENDIX  
PROOF OF CONVERGENCE

For a function  $f(\mathbf{x}, \mathbf{z})$ , we denote the vector  $(\nabla_{\mathbf{x}}f, \nabla_{\mathbf{z}}f)$  in short by  $\nabla_{\mathbf{x}, \mathbf{z}}f$ . We give a brief proof for Theorem 1. Let's start with a few lemmas.

**Lemma 1:** The Clarke subdifferential of  $\|g^r(\mathbf{y})\|_{2,1}$ , where  $g^r(\cdot) \in \mathbb{R}^{m_r \times d_r}$  and  $r$  is either  $R$  or  $Q$  defined in equation (9), is as follows:

$$\partial^c \|g^r(\mathbf{y})\|_{2,1} = \left\{ \sum_{i \in I_0} \nabla g_i^r(\mathbf{y})^\top \mathbf{w}_i + \sum_{i \in I_1} \nabla g_i^r(\mathbf{y})^\top \frac{g_i^r(\mathbf{y})}{\|g_i^r(\mathbf{y})\|} \mid \mathbf{w}_i \in \mathbb{R}^{d_r}, \|\Pi(\mathbf{w}_i; \mathcal{C}(\nabla g_i^r(\mathbf{y})))\| \leq 1, \forall i \in I_0 \right\}, \quad (23)$$

where  $I_0 = \{i \in [m_r] \mid \|g_i^r(\mathbf{y})\| = 0\}$ ,  $I_1 = [m_r] \setminus I_0$ , and  $\Pi(\mathbf{w}; \mathcal{C}(\mathbf{A}))$  is the projection of  $\mathbf{w}$  onto  $\mathcal{C}(\mathbf{A})$  which stands for the column space of  $\mathbf{A}$ .

**Lemma 2:** The gradient  $\nabla r_\varepsilon(\mathbf{y})$  in equation (11) is  $(\sqrt{m}L_{g^r} + \frac{M^2}{\varepsilon})$ -Lipschitz continuous, where  $L_{g^r}$  is the Lipschitz constant of  $\nabla g^r$  and  $M = \sup_y \|\nabla g^r(y)\|_2$ . Consequently,  $\nabla_{\mathbf{x}, \mathbf{z}}\Phi_\varepsilon(\mathbf{x}, \mathbf{z})$  is  $L_\varepsilon$ -Lipschitz continuous with  $L_\varepsilon = O(\varepsilon^{-1})$ .

The proofs of Lemmas 1-2 can be found in Lemmas 3.1-3.2 in [15].

**Lemma 3:** Let  $\Phi_\varepsilon(\mathbf{x}, \mathbf{z})$  be defined in equation (14), and  $(\mathbf{x}_0, \mathbf{z}_0) \in X \times Z$  be arbitrary. Suppose  $\{\mathbf{x}_k, \mathbf{z}_k\}$  is the sequence generated by repeating Lines 2–10 of Algorithm 1 with  $\varepsilon_k = \varepsilon$ . Then  $\|\nabla\Phi_\varepsilon(\mathbf{x}_k, \mathbf{z}_k)\| \rightarrow 0$  as  $k \rightarrow \infty$ .

**Proof:** Given  $(\mathbf{x}_k, \mathbf{z}_k)$ , in case that  $(\mathbf{x}_{k+1}, \mathbf{z}_{k+1}) = (\mathbf{v}_{k+1}^{\mathbf{x}}, \mathbf{v}_{k+1}^{\mathbf{z}})$ , and condition (13) holds after backtracking for  $\ell_k \geq 0$  times. Then, the algorithm computes

$$\mathbf{v}_{k+1}^{\mathbf{x}} = \mathbf{x}_k - \bar{\alpha}\rho^{\ell_k} \nabla_{\mathbf{x}}\Phi_\varepsilon(\mathbf{x}_k, \mathbf{z}_k), \quad (24)$$

$$\mathbf{v}_{k+1}^{\mathbf{z}} = \mathbf{z}_k - \bar{\beta}\rho^{\ell_k} \nabla_{\mathbf{z}}\Phi_\varepsilon(\mathbf{v}_{k+1}^{\mathbf{x}}, \mathbf{z}_k). \quad (25)$$

By the  $L_\varepsilon$ -Lipschitz continuity of  $\nabla_{\mathbf{x}, \mathbf{z}}\Phi_\varepsilon$  and equations above, we have

$$\begin{aligned} \Phi_\varepsilon(\mathbf{v}_{k+1}^{\mathbf{x}}, \mathbf{v}_{k+1}^{\mathbf{z}}) &\leq \Phi_\varepsilon(\mathbf{v}_{k+1}^{\mathbf{x}}, \mathbf{z}_k) \\ &+ \nabla_{\mathbf{z}}\Phi_\varepsilon(\mathbf{v}_{k+1}^{\mathbf{x}}, \mathbf{z}_k) \cdot (\mathbf{v}_{k+1}^{\mathbf{z}} - \mathbf{z}_k) + \frac{L_\varepsilon}{2} \|\mathbf{v}_{k+1}^{\mathbf{z}} - \mathbf{z}_k\|^2 \\ &\leq \Phi_\varepsilon(\mathbf{x}_k, \mathbf{z}_k) + \nabla_{\mathbf{x}}\Phi_\varepsilon(\mathbf{x}_k, \mathbf{z}_k) \cdot (\mathbf{v}_{k+1}^{\mathbf{x}} - \mathbf{x}_k) \\ &+ \frac{L_\varepsilon}{2} \|\mathbf{v}_{k+1}^{\mathbf{x}} - \mathbf{x}_k\|^2 + \nabla_{\mathbf{z}}\Phi_\varepsilon(\mathbf{v}_{k+1}^{\mathbf{x}}, \mathbf{z}_k) \cdot (\mathbf{v}_{k+1}^{\mathbf{z}} - \mathbf{z}_k) \\ &+ \frac{L_\varepsilon}{2} \|\mathbf{v}_{k+1}^{\mathbf{z}} - \mathbf{z}_k\|^2 \\ &\leq \Phi_\varepsilon(\mathbf{x}_k, \mathbf{z}_k) + \left(-\frac{1}{\bar{\alpha}\rho^{\ell_k}} + \frac{L_\varepsilon}{2}\right) \|\mathbf{v}_{k+1}^{\mathbf{x}} - \mathbf{x}_k\|^2 \\ &+ \left(-\frac{1}{\bar{\beta}\rho^{\ell_k}} + \frac{L_\varepsilon}{2}\right) \|\mathbf{v}_{k+1}^{\mathbf{z}} - \mathbf{z}_k\|^2. \end{aligned} \quad (26)$$

Hence, for any  $k = 1, 2, \dots$  the maximum line search steps  $\ell_{max}$  required for equation (21) satisfies  $\rho^{\ell_{max}} = (\delta + L_\varepsilon/2)^{-1}(\max\{\bar{\alpha}, \bar{\beta}\})^{-1}$ . Note that  $0 \leq \ell_k \leq \ell_{max}$ , hence,

$$\min\{\bar{\alpha}, \bar{\beta}\}\rho^{\ell_k} \geq \min\{\bar{\alpha}, \bar{\beta}\}(\delta + L_\varepsilon/2)^{-1}(\max\{\bar{\alpha}, \bar{\beta}\})^{-1}. \quad (27)$$

Moreover, from equation (24) we know that when the condition in equation (21) is met, we have

$$\begin{aligned} &\Phi_\varepsilon(\mathbf{v}_{k+1}^{\mathbf{x}}, \mathbf{v}_{k+1}^{\mathbf{z}}) - \Phi_\varepsilon(\mathbf{x}_k, \mathbf{z}_k) \\ &\leq -\delta(\bar{\alpha}\rho^{\ell_k})^2 \|\nabla_{\mathbf{x}}\Phi_\varepsilon(\mathbf{x}_k, \mathbf{z}_k)\|^2 \\ &\quad - \delta(\bar{\beta}\rho^{\ell_k})^2 \|\nabla_{\mathbf{z}}\Phi_\varepsilon(\mathbf{v}_{k+1}^{\mathbf{x}}, \mathbf{z}_k)\|^2. \end{aligned} \quad (28)$$

Now we estimate the last term in equation (28). Using  $L_\varepsilon$ -Lipschitz of  $\nabla_{\mathbf{x}, \mathbf{z}}\Phi_\varepsilon$  and the inequality  $b^2 \geq \mu a^2 - \frac{\mu}{1-\mu}(a-b)^2$  for all  $\mu \in (0, 1)$ , we get

$$\begin{aligned} &\|\nabla_{\mathbf{z}}\Phi_\varepsilon(\mathbf{v}_{k+1}^{\mathbf{x}}, \mathbf{z}_k)\|^2 - \mu \|\nabla_{\mathbf{z}}\Phi_\varepsilon(\mathbf{x}_k, \mathbf{z}_k)\|^2 \\ &\geq -\frac{\mu}{1-\mu} \|\nabla_{\mathbf{z}}\Phi_\varepsilon(\mathbf{v}_{k+1}^{\mathbf{x}}, \mathbf{z}_k) - \nabla_{\mathbf{z}}\Phi_\varepsilon(\mathbf{x}_k, \mathbf{z}_k)\|^2 \\ &\geq -\frac{\mu}{1-\mu} L_\varepsilon^2 \|\mathbf{v}_{k+1}^{\mathbf{x}} - \mathbf{x}_k\|^2 \\ &= -\frac{\mu}{1-\mu} L_\varepsilon^2 (\bar{\alpha}\rho^{\ell_k})^2 \|\nabla_{\mathbf{x}}\Phi_\varepsilon(\mathbf{x}_k, \mathbf{z}_k)\|^2. \end{aligned} \quad (29)$$

Inserting equation (29) into equation (28), we have

$$\begin{aligned} &\Phi_\varepsilon(\mathbf{v}_{k+1}^{\mathbf{x}}, \mathbf{v}_{k+1}^{\mathbf{z}}) - \Phi_\varepsilon(\mathbf{x}_k, \mathbf{z}_k) \\ &\leq -\delta\mu(\bar{\beta}\rho^{\ell_k})^2 \|\nabla_{\mathbf{z}}\Phi_\varepsilon(\mathbf{x}_k, \mathbf{z}_k)\|^2 \\ &\quad - \delta(\bar{\alpha}\rho^{\ell_k})^2 \left(1 - \frac{\mu}{1-\mu} (\bar{\beta}\rho^{\ell_k})^2 L_\varepsilon^2\right) \|\nabla_{\mathbf{x}}\Phi_\varepsilon(\mathbf{x}_k, \mathbf{z}_k)\|^2. \end{aligned} \quad (30)$$

Then from equation (27) and equation (30), there are a sufficiently small  $\mu$  and a constant  $C_1 > 0$ , depending only on  $\rho, \delta, \bar{\alpha}, \bar{\beta}$ , such that

$$\|\nabla_{\mathbf{x}, \mathbf{z}}\Phi_\varepsilon(\mathbf{x}_k, \mathbf{z}_k)\|^2 \leq C_1 L_\varepsilon^2 (\Phi_\varepsilon(\mathbf{x}_k, \mathbf{z}_k) - \Phi_\varepsilon(\mathbf{v}_{k+1}^{\mathbf{x}}, \mathbf{v}_{k+1}^{\mathbf{z}})). \quad (31)$$

On the other hand, in case that we can take  $(\mathbf{x}_{k+1}, \mathbf{z}_{k+1}) = (\mathbf{u}_{k+1}^{\mathbf{x}}, \mathbf{u}_{k+1}^{\mathbf{z}})$ , then the conditions in (10a-b) hold. Hence in any case we have

$$\begin{aligned} &\Phi_\varepsilon(\mathbf{x}_{k+1}, \mathbf{z}_{k+1}) - \Phi_\varepsilon(\mathbf{x}_k, \mathbf{z}_k) \\ &\leq -C_2 \left( \|\mathbf{x}_{k+1} - \mathbf{x}_k\|^2 + \|\mathbf{z}_{k+1} - \mathbf{z}_k\|^2 \right), \\ &\|\nabla\Phi_\varepsilon(\mathbf{x}_k, \mathbf{z}_k)\|^2 \leq C_3 (\Phi_\varepsilon(\mathbf{x}_k, \mathbf{z}_k) - \Phi_\varepsilon(\mathbf{v}_{k+1}^{\mathbf{x}}, \mathbf{v}_{k+1}^{\mathbf{z}})), \end{aligned} \quad (32)$$

$$\quad (33)$$

where  $C_2 = \min\{\eta, \delta\}$ ,  $C_3 = \max\{2/\eta^3, C_1 L_\varepsilon^2\}$ . From equation (32), It is easy to conclude that there is a  $\Phi_\varepsilon^*$ , such that  $\nabla\Phi_\varepsilon(\mathbf{x}_k, \mathbf{z}_k) \downarrow \Phi_\varepsilon^*$  as  $k \rightarrow \infty$ . Then adding up both sides of equation (33) w.r.t.  $k$ , it yields that for any  $K$ ,  $\sum_{k=0}^K \|\nabla\Phi_\varepsilon(\mathbf{x}_k, \mathbf{z}_k)\|^2 \leq C_3 (\Phi_\varepsilon(\mathbf{x}_0, \mathbf{z}_0) - \Phi_\varepsilon^*)$ . This leads to the conclusion of the lemma immediately.

**Proof of Theorem 1:** By using the above three lemmas the theorem can be proved by the argument similar to Theorem 3.6 in [15].

REFERENCES

- [1] H. Shan *et al.*, "Competitive performance of a modularized deep neural network compared to commercial algorithms for low-dose CT image reconstruction," *Nature Machine Intelligence*, vol. 1, pp. 269–276, June 2019.
- [2] C. Ding, Q. Zhang, G. Wang, X. Ye, and Y. Chen "Learned alternating minimization algorithm for dual-domain sparse view CT reconstruction," *Proc. Int. Conf. Med. Image Comput. Comput.-Assist. Intervent.* Cham, Switzerland: Springer, 2023, vol. 14229, pp. 173–183.
- [3] Z. Zhang, X. Liang, X. Dong, Y. Xie, and G. Cao "A sparse-view CT reconstruction method based on combination of densenet and deconvolution" *IEEE Trans. Med. Imag.*, vol. 37, no. 6, pp. 1407–1417, June 2018.

- [4] D. H. Ye, G. T. Buzzard, M. Ruby, and Ch. A. Bouman “Deep back projection for sparse-view CT reconstruction”, *2018 IEEE Global Conference on Signal and Information Processing (GlobalSIP)*, Anaheim, CA, USA, 2018, pp. 1-5, Feb. 2019.
- [5] H. Lee, J. Lee, H. Kim, B. Cho and S. Cho, “Deep-Neural-Network-Based Sinogram Synthesis for Sparse-View CT Image Reconstruction,” in *IEEE Trans. Radiat. Plasma Med. Sci.*, vol. 3, no. 2, pp. 109-119, Mar. 2019.
- [6] D. Hu et al., “Hybrid-Domain Neural Network Processing for Sparse-View CT Reconstruction,” in *IEEE Trans. Radiat. Plasma Med. Sci.*, vol. 5, no. 1, pp. 88-98, Jan. 2021
- [7] L. Yang, R. Ge, S. Feng, and D. Zhang “Learning projection views for sparse-view ct reconstruction,” in *Proc. of the 30th ACM Int. Conf. on Multimedia*, pp. 2645– 2653, Oct. 2022.
- [8] D. Yarotsky, “Error bounds for approximations with deep ReLU networks,” *Neural Networks*, vol. 94, pp. 103–114, Oct. 2017.
- [9] K. Hornik, M. Stinchcombe, and H. White, “Multilayer feedforward networks are universal approximators,” *Neural Networks*, vol. 2, no. 5, pp. 359–366, 1989.
- [10] S. Liang and R. Srikant, “Why deep neural networks for function approximation?” in *Proc. Int. Conf. Learning Repr. (ICLR)*, 2017.
- [11] J. Zhang and B. Ghanem, “Ista-net: Interpretable optimization-inspired deep network for image compressive sensing,” in *Proc. IEEE/CVF Conf. Comput. Vis. Pattern Recognit. (CVPR)*, pp. 1828–1837, 2018.
- [12] V. Monga, Y. Li, and Y. C. Eldar, “Algorithm unrolling: Interpretable, efficient deep learning for signal and image processing,” *IEEE Signal Process. Mag.*, vol. 38, no. 2, pp. 18–44, Mar. 2021.
- [13] H. Chen et al., “Learn: Learned experts’ assessment-based reconstruction network for sparse-data CT,” *IEEE Trans. Med. Imag.*, vol. 37, no. 6, pp. 1333–1347, June 2018.
- [14] Y. Zhang et al., “Learn++: Recurrent dual-domain reconstruction network for compressed sensing CT,” *IEEE Trans. Radiat. Plasma Med. Sci.*, vol. 7, no. 2, pp. 132–142, Feb. 2023.
- [15] Y. Chen et al., “Learnable descent algorithm for nonsmooth nonconvex image reconstruction,” *SIAM J. Imag. Sci.*, vol. 14, no. 4, pp. 1532–1564, 2021.
- [16] H. Chen et al., “Low-dose CT with a residual encoder-decoder convolutional neural network,” *IEEE Trans. Med. Imag.*, vol. 36, no. 12, pp. 2524–2535, Dec. 2017.
- [17] K. H. Jin et al., “Deep convolutional neural network for inverse problems in imaging,” *IEEE Trans. Image Process.*, vol. 26, no. 9, pp. 4509–4522, Sept. 2017.
- [18] Z. Zhang et al., “A sparse-view CT reconstruction method based on combination of DenseNet and deconvolution,” *IEEE Trans. Med. Imag.*, vol. 37, no. 6, pp. 1407–1417, June 2018.
- [19] J. Zhang, Y. Hu, J. Yang, Y. Chen, J.-L. Coatrieux, and L. Luo, “Sparse-view X-ray CT reconstruction with gamma regularization,” *Neurocomputing*, vol. 230, pp. 251–269, Mar. 2017.
- [20] W. Xia, Z. Yang, Q. Zhou, Z. Lu, Z. Wang, and Y. Zhang, “A transformer-based iterative reconstruction model for sparse-view CT reconstruction,” in *Proc. Int. Conf. Med. Image Comput. Comput.-Assist. Intervent.* Cham, Switzerland: Springer, 2022, pp. 790–800.
- [21] H. Lee, J. Lee, H. Kim, B. Cho, and S. Cho, “Deep-neural-network-based sinogram synthesis for sparse-view CT image reconstruction,” *IEEE Trans. Radiat. Plasma Med. Sci.*, vol. 3, no. 2, pp. 109–119, Mar. 2019.
- [22] L. Yang, Z. Li, R. Ge, J. Zhao, H. Si, and D. Zhang, “Low-dose CT denoising via sinogram inner-structure transformer,” *IEEE Trans. Med. Imag.*, vol. 42, no. 4, pp. 910–921, Apr. 2023.
- [23] L. Yu, Z. Zhang, X. Li, and L. Xing, “Deep sinogram completion with image prior for metal artifact reduction in CT images,” *IEEE Trans. Med. Imag.*, vol. 40, no. 1, pp. 228–238, Jan. 2021.
- [24] W. Wu, D. Hu, C. Niu, H. Yu, V. Vardhanabhuti, and G. Wang, “DRONE: Dual-domain residual-based optimization network for sparse-view CT reconstruction,” *IEEE Trans. Med. Imag.*, vol. 40, no. 11, pp. 3002–3014, Nov. 2021.
- [25] B. Zhou, X. Chen, H. Xie, S. K. Zhou, J. S. Duncan, and C. Liu, “DU-DOUFNET: Dual-domain under-to-fully-complete progressive restoration network for simultaneous metal artifact reduction and low-dose CT reconstruction,” *IEEE Trans. Med. Imag.*, vol. 41, no. 12, pp. 3587–3599, Dec. 2022.
- [26] R. Ge et al., “DDPNET: A novel dual-domain parallel network for low-dose CT reconstruction,” in *Proc. Int. Conf. Med. Image Comput. Comput.-Assist. Intervent.* Cham, Switzerland: Springer, 2022, pp. 748–757.
- [27] J. Bolte, S. Sabach, and M. Teboulle, “Proximal alternating linearized minimization for nonconvex and nonsmooth problems,” *Mathematical Programming*, vol. 146, no. 1-2, pp. 459–494, Aug. 2014.
- [28] T. Pock and S. Sabach, “Inertial proximal alternating linearized minimization (ipalm) for nonconvex and nonsmooth problems,” *SIAM Journal on Imag. Sci.*, vol. 9, no. 4, pp. 1756–1787, 2016.
- [29] B. T. Polyak, “Some methods of speeding up the convergence of iteration methods,” *USSR Computational Mathematics and Mathematical Physics*, vol. 4, no. 5, pp. 1–17, 1964.
- [30] Y. Nesterov, “Lectures on Convex Optimization, 2nd ed.,” *Springer Publishing Company, Incorporated*, 2018.
- [31] Y. Yang, J. Sun, H. Li, and Z. Xu, “Deep ADMM-Net for compressive sensing MRI,” in *Advances in Neural Information Processing Systems*, vol. 29, 2016.
- [32] Y. Kim, H. Jung, D. Min, and K. Sohn, “Deeply aggregated alternating minimization for image restoration,” in *Proc. IEEE/CVF Conf. Comput. Vis. Pattern Recognit. (CVPR)*, pp. 284–292, 2017.
- [33] Y. Chun and J. A. Fessler, “Deep BCD-Net using identical encoding-decoding CNN structures for iterative image recovery,” in *2018 IEEE 13th Image, Video, and Multidimensional Signal Processing Workshop (IVMSP)*, pp. 1–5, 2018.
- [34] S. Mukherjee, A. Hauptmann, O. Oktem, M. Pereyra, and C.-B. Schönlieb, “Learned reconstruction methods with convergence guarantees: a survey of concepts and applications,” *IEEE Signal Processing Magazine*, vol. 40, no. 1, pp. 164–182, Jan. 2023.
- [35] I. Y. Chun and J. A. Fessler, “Convolutional analysis operator learning: acceleration and convergence,” *IEEE Trans. on Image Process.*, vol. 29, pp. 2108–2122, 2020.
- [36] A. Gkillas, D. Ampeliotis, and K. Berberidis, “Connections between deep equilibrium and sparse representation models with application to hyperspectral image denoising,” *IEEE Trans. on Image Process.*, vol. 32, pp. 1513–1528, 2023.
- [37] Y. Sun, Z. Wu, X. Xu, B. Wohlberg, and U. S. Kamilov, “Scalable plug-and-play ADMM with convergence guarantees,” *IEEE Trans. on Comp. Imag.*, vol. 7, pp. 849–863, 2021.
- [38] I. Chun, Z. Huang, H. Lim, and J. A. Fessler, “Momentum-Net: Fast and convergent iterative neural network for inverse problems,” *IEEE Trans. Pattern Anal. Mach. Intell.*, vol. 45, no. 4, pp. 4915–4931, Apr. 2023.
- [39] K. He, X. Zhang, S. Ren, and J. Sun, “Deep residual learning for image recognition,” *arXiv:1512.0338*, 2015.
- [40] Y. Nesterov, “Smooth minimization of non-smooth functions,” *Mathematical Programming*, vol. 103, no. 1, pp. 127–152, Dec. 2004.
- [41] Z. Zhang, X. Liang, X. Dong, Y. Xie, and G. Cao, “A sparse-view CT reconstruction method based on combination of DenseNet and deconvolution,” *IEEE Trans. on Med. Imag.*, vol. 37, no. 6, pp. 1407–1417, June 2018.
- [42] C. Wang, K. Shang, H. Zhang, Q. Li, Y. Hui, and S. K. Zhou, “DUDO-TRANS: Dual-domain transformer provides more attention for sinogram restoration in sparse-view CT reconstruction,” *arXiv:2111.10790*, 2021.
- [43] Z. Wang, A. C. Bovik, H. R. Sheikh, and E. P. Simoncelli, “Image quality assessment: from error visibility to structural similarity,” *IEEE Trans. on Image Process.*, vol. 13, no. 4, pp. 600–612, Apr. 2004.
- [44] B. De Man and S. Basu, “Distance-driven projection and backprojection in three dimensions,” *Physics in Medicine and Biology*, vol. 49, no. 11, pp. 2463–2475, May 2004.
- [45] W. Xia, Z. Lu, Y. Huang, Z. Shi, Y. Liu, H. Chen, Y. Chen, J. Zhou, and Y. Zhang, “MAGIC: Manifold and graph integrative convolutional network for low-dose CT reconstruction,” *IEEE Trans. on Med. Imag.*, vol. 40, no. 12, pp. 3459–3472, Dec. 2021.
- [46] D. P. Kingma and J. Ba, “Adam: A method for stochastic optimization,” *arXiv:1412.6980*, Jan. 2017.
- [47] V. Antun, F. Renna, C. Poon, B. Adcock, and A. C. Hansen, “On instabilities of deep learning in image reconstruction and the potential costs of AI,” *Proceedings of the National Academy of Sciences*, vol. 117, no. 48, pp. 30088–30095, Mar. 2020.